THE ASTROPHYSICAL JOURNAL, 446:622–636, 1995 June 20

UIT AND OPTICAL IMAGERY OF LARGE MAGELLANIC CLOUD ASSOCIATIONS LH 52 AND LH 53: AGES AND INITIAL MASS FUNCTION SLOPES

ROBERT S. HILL,[1] K.-P. CHENG,[1,2] RALPH C. BOHLIN,[3] ROBERT W. O'CONNELL,[4] MORTON S. ROBERTS,[5] ANDREW M. SMITH,[6] AND THEODORE P. STECHER[6]

Received 1994 September 28; accepted 1994 December 30

ABSTRACT

A 40′ field including the stellar associations LH 52 and LH 53 and the supernova remnant N49 in the Large Magellanic Cloud was observed by the Ultraviolet Imaging Telescope (UIT) during the Astro-1 Space Shuttle mission in 1990 December. The image in the 162 nm bandpass is discussed together with ground-based *BV* data on subfields containing LH 52 and LH 53. Point-spread function photometry in the 162 nm, *B*, and *V* bands is presented in the form of color-magnitude diagrams and two-color diagrams, which are compared with stellar models. The far-ultraviolet extinction curve of the dust in LH 52 is unusually steep for the LMC. The most probable age of both associations is ~ 10 Myr, which constrains the scenario for the evolution of the supergiant Hα shell LMC 4 by stochastic self-propagated star formation. The initial mass function (IMF) slope for LH 52 is $\Gamma \approx -1$, in agreement with previous work, and the slope for LH 53, which is less densely populated, is $\Gamma \approx -2$. A similar relationship between surface density of stars and IMF slope is reported for a UIT field near 30 Dor. The ultraviolet morphology of N49, which is contained in LH 53, is dominated by two bright features that straddle an X-ray bright spot, consistent with an encounter between the blast wave and a cloud. The estimated age of ~ 10 Myr for LH 53 implies an initial mass of $\sim 20\ M_\odot$ for the N49 progenitor star.

Subject headings: dust, extinction — Magellanic Clouds — open clusters and associations: individual (LH 52, LH 53) — stars: luminosity function, mass function — ultraviolet: stars

1. INTRODUCTION

A field in the northeast LMC on the edge of supergiant Hα shell LMC 4 (Goudis & Meaburn 1978) was observed by the Ultraviolet Imaging Telescope (UIT) during the Astro-1 Space Shuttle mission in 1990 December. The field contains the supernova remnant (SNR) N49 and the two cataloged OB associations LH 52 and LH 53 (Lucke & Hodge 1970).

Like globular and open clusters, OB associations are best studied through the photometry and spectroscopy of a fair sample of the constituent stars, resulting in color-magnitude (*C-M*) diagrams and two-color (2-C) diagrams. However, establishing the membership of stars in associations is more difficult than for clusters. The chief problem is the low contrast of an association relative to the general field. Nearby associations may cover several square degrees, and their boundaries are drawn using OB stars only. The individual membership of a moderate or low-mass main-sequence star is practically impossible to determine, and statistical methods must be used to correct the observed *C-M* diagram for field-star contamination in this range. The problem is somewhat less in nearby external galaxies. In particular, the LMC offers a large number of fairly well delineated associations which are the subject of a growing body of work by several groups (Garmany 1994).

As samples of a young stellar population, OB associations are usefully studied at ultraviolet as well as optical wavelengths. Wide-field ultraviolet imagery has a high value in clearly showing the spatial distribution of the youngest and most massive stars. Both the internal structure of an association and its relationship to the early-type stars in the field are seen. In addition, excellent temperature discrimination in the range 10,000–30,000 K is offered by ultraviolet-optical colors; e.g., the difference between a B0 and an A0 star is a mere 0.3 mag in $B-V$, but it is ~ 4 mag in a color index $m_{160} - V$, where m_{160} is the monochromatic magnitude at a wavelength of 160 nm (Fanelli et al. 1992). Moreover, significant variations in the reddening curve are observed most easily in the ultraviolet.

This paper is primarily concerned with the estimation of initial mass function (IMF) slopes and ages for LH 52 and LH 53. Our results are compared to those obtained for LH 52 by Vallenari, Bomans, & deBoer (1993, hereafter VBD93), who kindly supplied a table of their photometric data. Also discussed is the character of the extinction curve of the dust in LH 52. These analyses require the comparison of results from stellar photometry with estimates based on theoretical isochrones. In order to avoid repetition, we note here that all the isochrones in this paper are taken from the convective overshoot models of Schaerer et al. (1993) for $Z = 0.008$. The transformation to the observational plane is done through the stellar atmosphere models of Kurucz (1992) with $\log Z/Z_\odot = -0.3$. These metallicities are chosen to agree as closely as possible with the average value $Z = 0.5\ Z_\odot$ given by Westerlund

[1] Hughes STX Corporation, Code 681, NASA/Goddard Space Flight Center, Greenbelt, MD 20071.
[2] Present address: Department of Physics, California State University, Fullerton, CA 92634.
[3] Space Telescope Science Institute, 3700 San Martin Drive, Baltimore, MD 21218.
[4] University of Virginia, P.O. Box 3818, Charlottesville, VA 22903.
[5] National Radio Astronomy Observatory, Edgemont Road, Charlottesville, VA 22903.
[6] Laboratory for Astronomy and Solar Physics, Code 681, NASA/GSFC, Greenbelt, MD 20771.

(1990) for H II regions and OB stars in the LMC. We assume a distance modulus of 18.5 and a foreground Galactic reddening of $E(B-V) = 0.05$ (VBD93).

Although the main subject of this paper is stellar associations, the SNR N49 is also considered. The UIT observation of N49 was the first attempt to image this important SNR in the ultraviolet. Moreover, N49 is within LH 53, and so any conclusions about LH 53 may affect the interpretation of N49. In particular, the age computed for LH 53 gives an estimate of the initial mass of the N49 progenitor.

The contents of the paper are: § 1, introduction; § 2, observations; § 3, stellar photometry; § 4, *C-M* diagram and 2-C diagrams; § 5, IMFs; § 6, N49; § 7, conclusions.

2. OBSERVATIONS

UIT has two detectors, each of which consists of a two-stage image intensifier coupled to 70 mm Eastman Kodak IIa-O film by fiber optics. Detector A has a CsTe photocathode, which responds mainly to light of wavelengths 170–300 nm. Detector B has a CsI photocathode, which responds mainly to light of wavelengths 130–170 nm. Each detector also includes a set of filters with bandwidths of 10–40 nm (Stecher et al. 1992).

A field centered at $\alpha = 05^h26^m30^s$, $\delta = -66°03'26''$ (equinox J2000) was observed by UIT from Earth orbit on 1990 December 12 13:30 UT. Six exposures were obtained, as summarized in Table 1. Three exposures were taken with detector A and filter A3 ($\lambda_{peak} = 191$ nm) in order to detect the SNR N49 in C III]; however, the exposure times were too short to produce useful data in this bandpass. The image used for this paper is the longest exposure taken with detector B, i.e., FUV0570. Because the LMC was observed on the daylight side of the Shuttle orbit, these images were taken with the B5 filter, which excludes dayglow emission shortward of 145 nm. Quantities derived from B5 images are indicated with the subscript 162,

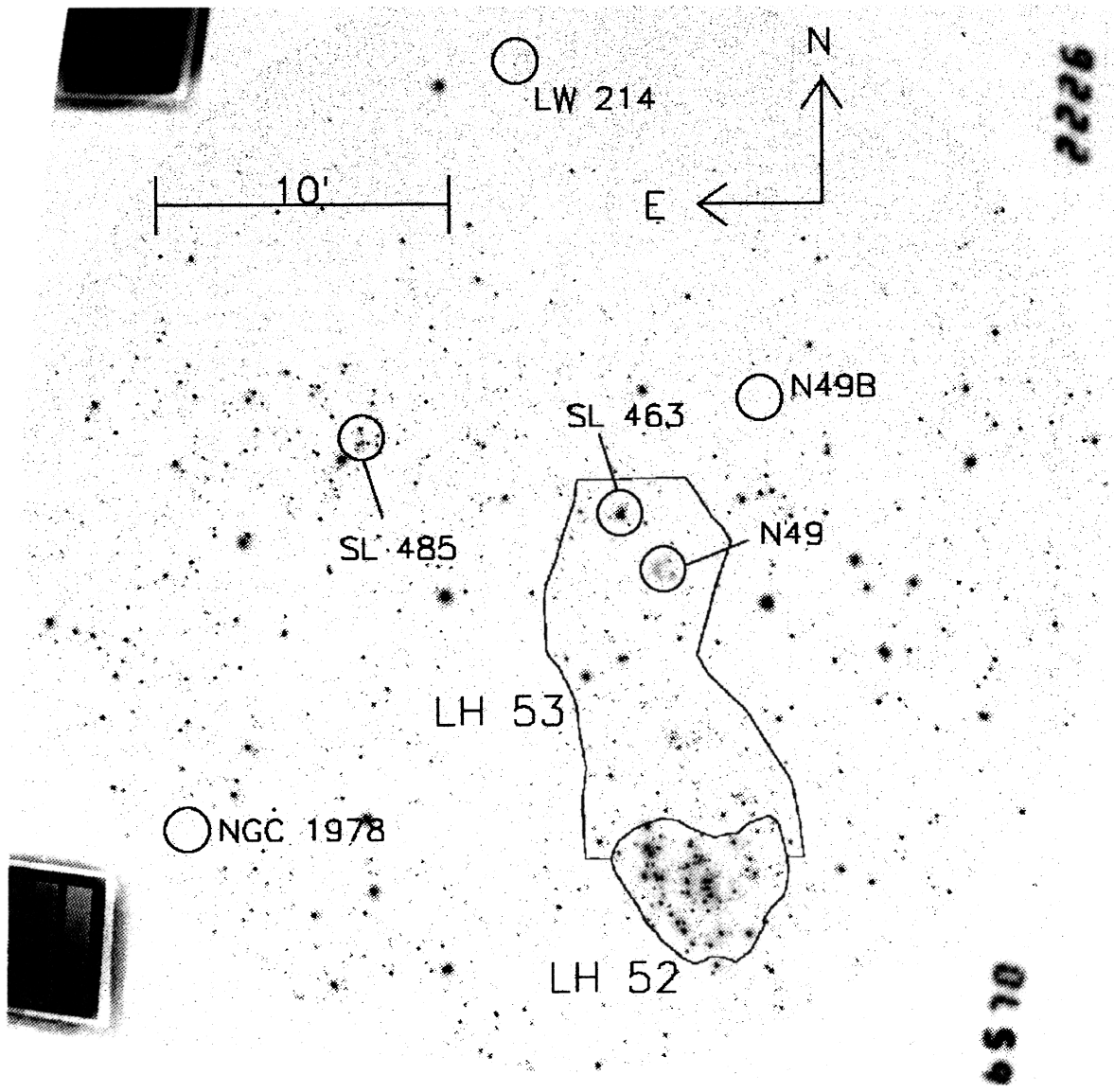

FIG. 1.—162 nm UIT image FUV0570; linear intensity scaling. Boundary of LH 52 is the same as in Lucke (1972). Boundary of LH 53 is shown as modified for this work. SL 463, SL 485, and LW 214 are open clusters (Hodge & Wright 1967). N49 and N49B are SNRs (Mathewson et al. 1983); N49B not detected by UIT. NGC 1978 is a globular cluster (Hodge & Wright 1967), not detected by UIT.

TABLE 1

OBSERVATIONS

Instrument[a]	Target	Exposure Time (s)	N[b]	Filter	$\bar{\lambda}$ (nm)	Date	Name
UIT	N49A + B	8.9	1	A3	196	1990 Dec 10	NUV0466
UIT	N49A + B	44.5	1	A3	196	1990 Dec 10	NUV0467
UIT	N49A + B	1.8	1	A3	196	1990 Dec 10	NUV0468
UIT	N49A + B	44.5	1	B5	162	1990 Dec 10	FUV0569
UIT	N49A + B	222.5	1	B5	162	1990 Dec 10	FUV0570
UIT	N49A + B	8.8	1	B5	162	1990 Dec 10	FUV0571
UIT	N49A + B	1.8	1	B5	162	1990 Dec 10	FUV0572
CTIO	LH 52	120.0	5	*B*	440	1992 Nov 23	LH52B
CTIO	LH 52	30.0	12	*V*	550	1992 Nov 21	LH52V
CTIO	LH 53	120.0	5	*B*	440	1992 Nov 23	LH53B
CTIO	LH 53	30.0	9	*V*	550	1992 Nov 21	LH53V

[a] UIT = Ultraviolet Imaging Telescope on Astro-1 Spacelab mission; CTIO = 36 inch telescope of Cerro Tololo Inter-American Observatory with Tek2048 CCD.

[b] If greater than 1, the number of images of the given exposure time combined by median filtering of each pixel among the input images.

which is the centroid wavelength of the filter response in nm; the bandwidth is 23 nm. Figure 1 shows image FUV0570 (220 s).

UIT images are digitized using a Perkin-Elmer 1010m microdensitometer. The pixel spacing and the aperture width are both set to 20 μm to produce a 2048 × 2048 array of density pixels for each image. Further processing is done by a software system called Batch Data Reduction (BDR), which is described briefly by Stecher et al. (1992) and more extensively by Hill, Hill, & Greason (1993b). The output of BDR is a flat-fielded digital image in linear flux units. The version of BDR used for this paper is called FLIGHT14 (flight 1, version 4). However, the calibration data for UIT have undergone a new analysis by members of the instrument team, resulting in changes to the data reduction. The ultraviolet magnitudes reported below are computed from FLIGHT14 flux images and corrected to match the new calibration.

Parts of this UIT field were also observed in *B* and *V* from Cerro Tololo Inter-American Observatory (CTIO) 1992 November 21–23 with the 0.9 m telescope. Several exposures were obtained in each bandpass and combined by taking the median of corresponding pixels in each image. One field covered LH 52, and the other covered the southern section of LH 53. The images were taken using the Tek2048 CCD with a plate scale of 0.″40 pixel^{-1}; the gain was 3.2 e^- ADU^{-1}, and the readout noise was 4.6 e^- pixel^{-1}. Seeing was ~2″. The observations are summarized in Table 1. The optical images and the measurements made on them are referred to as UIT supporting data.

3. STELLAR PHOTOMETRY

3.1. *Ultraviolet*

Photometry of the image FUV0570 has resulted in ultraviolet magnitudes for 122 stars in LH 52 and for 196 stars in LH 53.

Ultraviolet stellar photometry is done on the UIT flux images using a locally written adaptation of some algorithms from the software package DAOPHOT (Stetson 1987). The primary modification is to the computation of photometric error as a function of accumulated signal, which in the case of UIT differs markedly from the Poissonian model appropriate for CCD data. Our photometry follows the typical DAOPHOT sequence of operations: point-source detection with a modified Gaussian filter, aperture photometry, and simultaneous point-spread function (PSF) fitting of groups of overlapping stars. The absolute calibration of FUV0570 is computed from an *IUE* archive spectrum (SWP 39129) of the star Sk −66°88 in LH 52. We refer to the resulting magnitudes as $m_{162} \equiv -2.5 \log f_{162} - 21.1$, where f_{162} is the mean flux in the UIT B5 bandpass in ergs cm^{-2} s^{-1} Å^{-1}.

Our ultraviolet photometry is based on flux images from version FLIGHT14 of the UIT data reduction (§ 2). The magnitudes calculated from these images are corrected to agree with a recent reanalysis of the UIT calibration data. Figure 2 shows aperture magnitudes based on a test reduction of image FUV0570 plotted against the corresponding FLIGHT14 PSF magnitudes. The solid curve shows the relation used to correct the old magnitudes to the new calibration; the 1 σ scatter of points about this curve is ±0.08 mag. The primary effect of

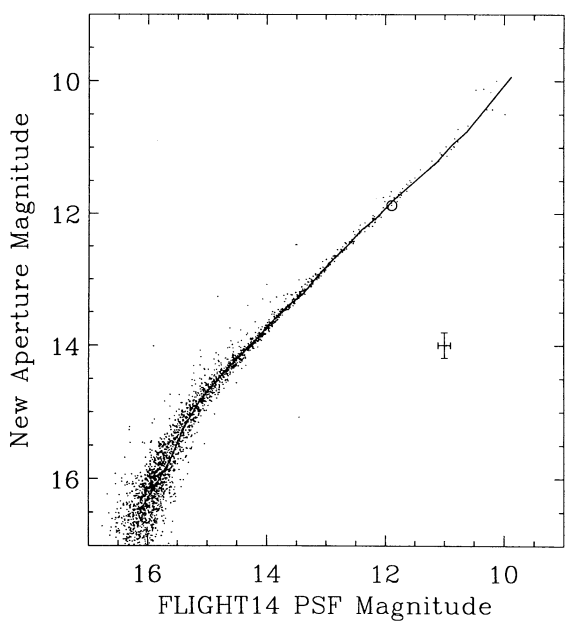

FIG. 2.—Calibration correction for PSF magnitudes based on a new UIT characteristic curve. *Abscissa*, PSF fit photometry from FLIGHT14 data reduction; *ordinate*, aperture photometry from preliminary version of new data reduction (FLIGHT15). Initially, each photometry set is calibrated separately using an *IUE* spectrum. The adopted correction is from the mean relation (*solid line*) computed by averaging the ordinate over 0.25 mag bins of the abscissa. *Circle*, Calibration star Sk −66°88, which is offset slightly from the mean relation for its magnitude bin. *Error bars*, Median internal errors from each type of photometry.

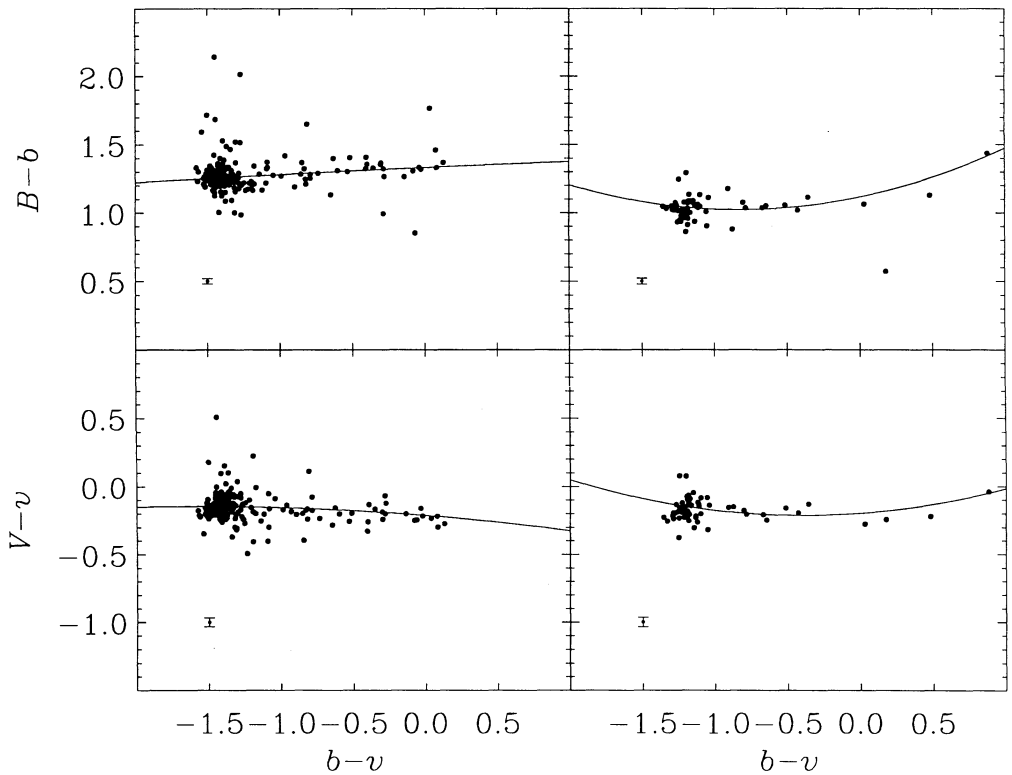

FIG. 3.—Calibration of UIT supporting data vs. the *BV* data of VBD93. *Left*, LH 52; *right*, LH 53. *Abscissa*, Instrumental color index ($b - v$); *ordinate*, difference between VBD93 magnitude (B or V) and the corresponding instrumental magnitude (b or v). Fitted quadratics are overplotted as lines. Error bars in each plot indicate the average of the errors used to weight the fit, i.e., the sum in quadrature of the internal error from our photometry and from that of VBD93 for each star.

the calibration correction is to make stars near $m_{162} = 14$ appear brighter by 0.2 mag. This in turn affects our interpretation by ruling out an extreme, SMC-like far-ultraviolet extinction curve for LH 52 (§ 4.1).

3.2. *Optical*

Stellar photometry is performed on the B and V images using the local software described above, except that the noise is treated in the way usual for CCDs. The calibration is done by fitting to the VBD93 photometry of LH 52 and part of LH 53. We use fitting functions of the form $V = v + \alpha_0 + \sum \alpha_i(b - v)^i$ and $B = b + \beta_0 + \sum \beta_i(b - v)^i$, where b and v are the raw PSF magnitudes, B and V are the magnitudes of VBD93 used as standards, and α and β are vectors of coefficients fitted using the singular value decomposition (SVD) method. By inspecting the residuals of trial fits, we choose 2 to be the degree of the polynomial. Only stars brighter than $V = 18$ are included. The fit is further restricted to measurements with small errors; i.e., only those stars are included for which the sum in quadrature of our error and VBD93 error is less than $0^m.07$ in the V band. The resulting calibrations are plotted in Figure 3.

3.3. *Ultraviolet and Optical Matching*

The cross-matching of stars between the ultraviolet image and the B images is done by inspection, because the correction for UIT magnetic focusing distortion is imperfectly determined (Greason et al. 1994). However, positions of sources in the B and the V images differ only by a constant (Δx, Δy) offset, so that a blind positional match can be done by a simple algo-

TABLE 2

TEN BRIGHTEST ULTRAVIOLET SOURCES IN LH 52

	COORDINATES (J2000)		m_{162}		B		V	
ID	α	δ	Mag	Error	Mag	Error	Mag	Error
4950.....	$05^h26^m05^s.44$	$-66°14'54''.0$	10.85	0.084	13.94	0.010	14.00	0.014
4920.....	05 26 06.66	−66 14 41.2	10.88	0.084	13.23	0.011	13.30	0.022
5060.....	05 26 07.60	−66 15 41.0	10.97	0.063	14.14	0.011	14.25	0.019
5301.....	05 25 31.73	−66 17 38.8	11.05	0.062	13.94	0.003	14.01	0.009
4817.....	05 26 06.82	−66 13 56.8	11.17	0.084	14.09	0.006	14.11	0.010
5131.....	05 25 45.25	−66 16 20.4	11.23	0.064	13.19	0.004	13.07	0.010
5064.....	05 26 01.88	−66 15 44.8	11.62	0.060	15.03	0.007	15.13	0.012
5297.....	05 25 53.78	−66 17 33.5	11.69	0.075	15.31	0.006	15.44	0.017
4880.....	05 25 37.33	−66 14 29.3	11.82	0.042	12.99	0.008	12.76	0.015
5255.....	05 25 56.11	−66 17 15.7	11.83	0.056	14.36	0.008	14.42	0.021

NOTE.—Complete ultraviolet and optical photometry for LH 52 is published in computer-readable form in the AAS CD-ROM Series, Vol. 5.

TABLE 3

TEN BRIGHTEST ULTRAVIOLET SOURCES IN LH 53

	COORDINATES (J2000)		m_{162}		B		V	
ID	α	δ	Mag	Error	Mag	Error	Mag	Error
4138.....	$05^h26^m27^s.61$	$-66°08'41''.8$	11.28	0.072	13.37	0.005	13.43	0.023
4072.....	05 26 15.79	−66 08 06.2	11.74	0.052	14.71	0.005	14.85	0.019
4896.....	05 26 23.08	−66 14 29.3	11.91	0.051	14.91	0.007	14.97	0.019
4756.....	05 25 41.06	−66 13 31.8	12.21	0.040	14.69	0.006	14.74	0.017
4867.....	05 25 17.83	−66 14 28.9	12.44	0.041	14.72	0.007	14.82	0.023
3421.....	05 26 29.75	−66 03 06.7	12.46	0.046	14.47	0.019	14.16	0.012
4601.....	05 26 19.24	−66 12 10.6	12.51	0.044	14.78	0.005	14.76	0.022
4700.....	05 25 34.11	−66 13 07.8	12.58	0.048	14.55	0.004	14.37	0.010
3974.....	05 25 56.26	−66 07 23.1	12.60	0.036	15.48	0.007	15.61	0.018
3894.....	05 26 07.62	−66 06 40.2	12.71	0.037	15.45	0.004	15.51	0.023

NOTE.—Complete ultraviolet and optical photometry for LH 53 is published in computer-readable form in the AAS CD-ROM Series, Vol. 5.

rithm. The maximum distance allowed between members of a matched pair is set at 2″, which is the approximate seeing. No inspection of individual optical sources is made, as so the only check on the reality of a source is the existence of a match.

For the LH 52 field, 3583 matches result from 3788 detections in V and 7656 detections in B. For the LH 53 field, 3585 matches result from 4072 detections in V and 6197 detections in B. The success rate in finding B matches for V detections in the areas observed in both bands is 0.95 for LH 52 and 0.92 for LH 53. Omission of stars outside the association boundaries leaves 1048 stars for LH 52 and 2227 stars for LH 53.

Tables 2 and 3 give m_{162}, B, and V for the 10 stars in each association that are the brightest at 162 nm. The complete ultraviolet and optical photometry of both associations is published in computer-readable form in the AAS CD-ROM Series, Vol. 5.

4. *C-M* DIAGRAMS AND 2-C DIAGRAMS

4.1. *LH 52 (NGC 1948)*

Figure 4 shows the *C-M* diagram in B and V of LH 52. All 1048 stars detected within the association boundary are included. This *C-M* diagram and the one shown in Figure 2 of VBD93 resemble each other except for the brighter limiting magnitude of the UIT supporting data. The sky area covered by the two *C-M* diagrams is also different, since our boundary corresponds to the one originally drawn by Lucke (1972). Overplotted on Figure 4 is a 10 Myr isochrone (§ 1), shifted by $E(B-V) = 0.15$ with a ratio of total to selective extinction, $A_V/E(B-V)$, of 3.1.

Two red supergiants in LH 52 have the anomalous trait that they are identified with ultraviolet sources. These stars are plotted as open circles in Figure 4 at $B-V \approx 1.6$. Their V magnitudes are 12.8 and 13.7, and their 162 nm magnitudes are 13.4 and 15.2, respectively. Apparently, different sources are seen on the UIT and the optical images. A red supergiant at the distance of the LMC cannot have the indicated ultraviolet magnitudes. Moreover, a hot star reddened to the indicated $B-V$ would not be detectable on the UIT images (Fanelli et al. 1992; Fitzpatrick 1985). With the present data, we cannot tell whether these anomalous matches are due to superposed sources or to physical binaries.

Magnitudes in the 162 nm, B, and V bands are combined to make both a 2-C diagram in the $(B-V, m_{162}-B)$-plane and a *C-M* diagram in the $(B-V, m_{162})$-plane. Figure 5 is a comparison of these diagrams with isochrones. The top row of plots shows the 2-C diagram, and the bottom row shows the *C-M* diagram. In order to avoid crowding, the observational data are plotted in duplicate on the left and right sides of the figure together with the 10 Myr and 20 Myr isochrones, respectively. These ages are the endpoints of the star formation interval computed by VBD93. In the 2-C versions of the isochrones, the main sequence and the supergiant branch are largely coincident. To facilitate comparison between the two types of diagram, an arbitrary group of stars with $m_{162} > 14$ and $|B-V| < 0.05$ are plotted as open circles, and all other stars are plotted as filled circles.

Figure 5 enables us to make a hypothesis about the far-ultraviolet extinction curve of the dust in LH 52. The plots include reddening vectors for $E(B-V) = 0.2$. These vectors are plotted from the bluest point on each isochrone. In the 2-C diagrams, the SMC-type reddening line nearly parallels the isochrone, whereas the LMC-type reddening line extends to

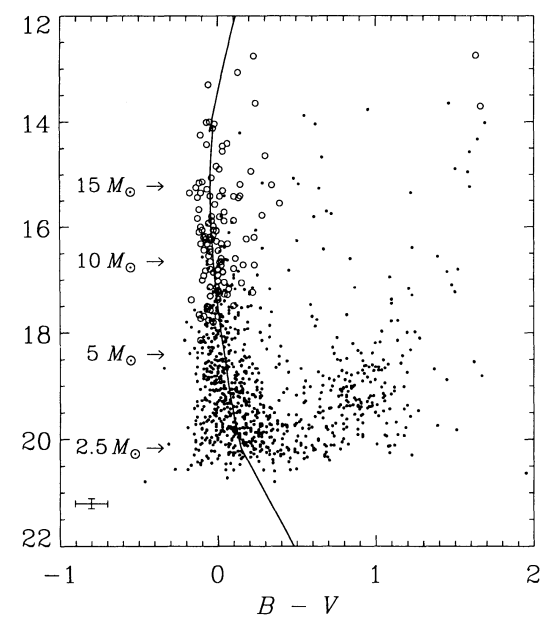

FIG. 4.—*C-M* diagram of LH 52 overplotted with 10 Myr isochrone from Schaerer et al. (1993), transformed to observational plane using Kurucz (1992) stellar atmosphere models and $E(B-V) = 0.15$. *Circles*, Stars cross-identified with 162 nm sources (the two at $B-V \approx 1.6$ are probably double; see text). *Error bars*, Average internal error from PSF photometry. Arrows are labeled with ZAMS masses along the isochrone.

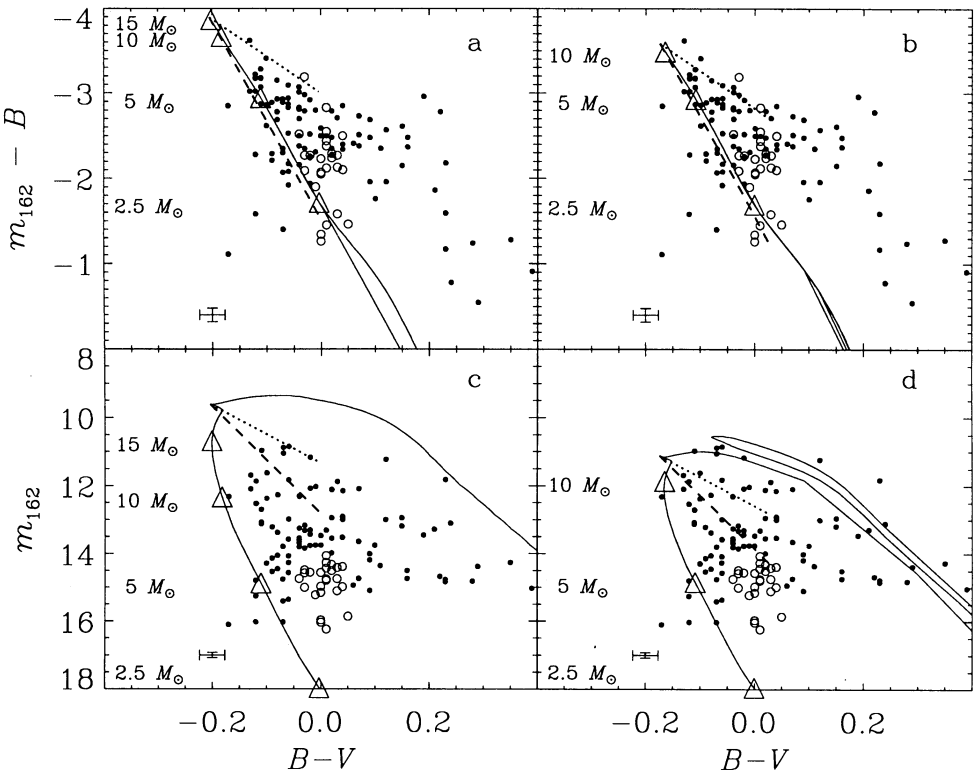

FIG. 5.—2-C diagram and *C-M* diagram of LH 52. *Top row*, $(B-V, m_{162}-B)$ 2-C diagram with (*a*) 10 Myr and (*b*) 20 Myr isochrones. *Bottom row*, $(B-V, m_{162})$ *C-M* diagram with (*c*) 10 Myr and (*d*) 20 Myr isochrones. *Open circles*, Arbitrary group of stars showing the relationship between the *C-M* diagram and the 2-C diagram. *Open triangles*, ZAMS masses given by the labels along the left edge inside each plot. *Error bars*, Mean internal errors from PSF photometry. *Dotted lines*, Reddening vectors for $E(B-V) = 0.2$, LMC reddening curve of Fitzpatrick (1985). *Dashed lines*, Reddening vectors for $E(B-V) = 0.2$, SMC reddening curve of Hutchings (1982).

the right. In order to be consistent with a particular type of reddening, a point must lie in the sector beneath the reddening line and to the right of the isochrone. Thus, SMC-type reddening is unlikely for LH 52, since many photometric points would lie to the right of the permitted sector for any age in the 10–20 Myr range.

An average reddening for LH 52 is computed from a subset of the main sequence. The relevant region of the optical *C-M* diagram is marked interactively using a mouse. Each of the stars in the resulting subset is moved to the 10 Myr isochrone along a reddening vector by an algorithm called MOVESTAR (§ 5.3). The length of each vector gives $E(B-V)$ for that star, and the mean of the $E(B-V)$-values is adopted for the association as a whole. Using a group of 421 stars with $14.8 \lesssim V \lesssim 18.6$ and $-0.20 \lesssim B-V \lesssim +0.15$, and neglecting field star contamination, we find that the $E(B-V)$ of LH 52 is 0.15 with a 1 σ scatter of ± 0.14 among the individual stars.

By an extension of this method, we can characterize the far-ultraviolet extinction, since we have measured some stars in all three bands (162 nm, *B*, and *V*). The parameter to be computed is $R_{162} \equiv A_{162}/E(B-V)$, where A_{162} is the total extinction at 162 nm. Either the 10 Myr or the 20 Myr isochrone, shifted to account for $E(B-V) = 0.05$ in the foreground, is used as the reference. The algorithm has three main steps: (1) MOVESTAR is used to compute an average reddening $E(B-V)_{BV}$ for the selected stars in the $(B-V, V)$-plane. (2) MOVESTAR is iterated several times with the same stars, but in the $(m_{162}-B, B)$-plane. For each iteration, a different value of R_{162} is used in the dereddening, and the average $E(B-V)$ is computed as before. The result is a relation between input values of R_{162} and output values of $E(B-V)$. (3) The value of R_{162} for the association is computed by interpolating in the relation obtained from step 2 at the reddening $E(B-V)_{BV}$ obtained from step 1.

In the $(B-V, V)$-plane, we find, for 108 stars with $B-V < 0.02$ and $V > 13.5$, that $E(B-V)_{BV} = 0.11$ using the 10 Myr isochrone, and that $E(B-V)_{BV} = 0.08$ using the 20 Myr isochrone. In the $(m_{162}-B, B)$-plane, we obtain the relations plotted in Figure 6, which shows the average $E(B-V)$ implied by a range of R_{162} for isochrones of 10 Myr and 20 Myr. Larger ages result in lower derived values of $E(B-V)$, since the isochrones move generally redward as the age increases. The values of R_{162} for some commonly used extinction curves are indicated by filled boxes. The error bars show the scatter (1 σ) in the $E(B-V)$-values computed in step 2 for individual stars in the 10 Myr case. The top and bottom sides of the outlined box denote the values of $E(B-V)_{BV}$ resulting from the application of step 1 for each of the two ages. The implied values of R_{162} are 12.80 (for 10 Myr) and 12.43 (for 20 Myr). Since a continuous range of stellar ages is likely to exist in the association, we adopt for LH 52 the values at the center of the box, i.e., $E(B-V) = 0.10$ and $R_{162} = 12.62$. Below, we apply this value of R_{162} to LH 53 as well.

The UIT calibration correction outlined above is essential for the proper computation of R_{162}. Without the correction, the UIT photometry implies that the LH 52 extinction curve is nearly as steep in the far-ultraviolet as that derived for the SMC by Hutchings (1982). Even with the correction, the curve

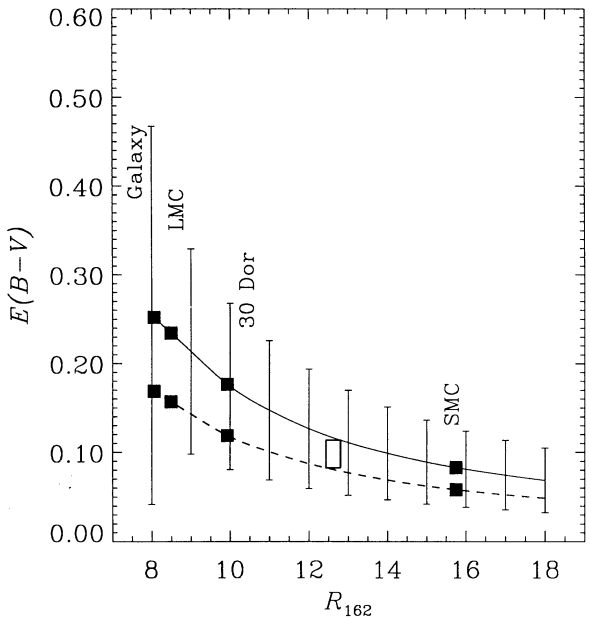

FIG. 6.—Reddening [$E(B-V)$] vs. normalized far-ultraviolet extinction in magnitudes (R_{162}) as constrained by stellar photometry of LH 52. B and 162 nm magnitudes are compared to theoretical isochrones shifted to account for a Galactic foreground extinction of $E(B-V) = 0.05$. The solid line results from an isochrone of age 10 Myr; the dashed line, 20 Myr. *Filled boxes*, R_{162} for some commonly used reddening curves, i.e., Galaxy (Savage & Mathis 1979), LMC (Fitzpatrick 1985), 30 Dor (Fitzpatrick 1985), and SMC (Hutchings 1982). *Error bars*, Scatter in $E(B-V)$-values among individual stars for 10 Myr case. *Outlined box*, Range of possible values as constrained by $E(B-V)$ measured from BV data alone.

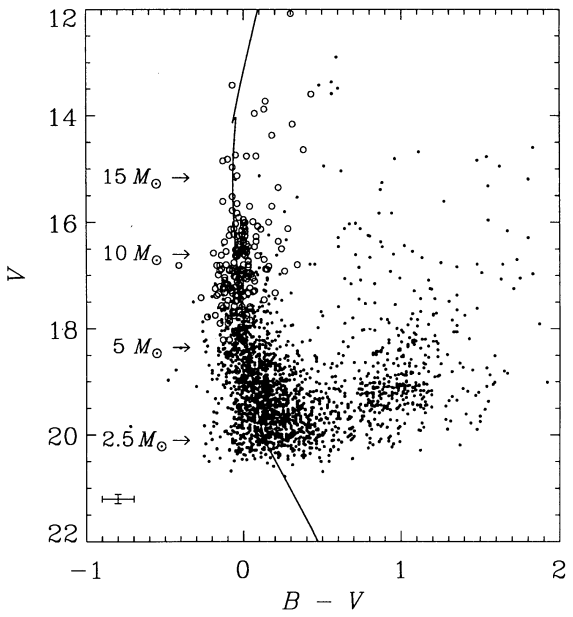

FIG. 7.—*C-M* diagram of LH 53 overplotted with 10 Myr isochrone from Schaerer et al. (1993), transformed to observational plane using Kurucz (1992) stellar atmosphere models and $E(B-V) = 0.14$. *Circles*, Stars cross-identified with 162 nm sources. *Error bars*, Average internal error from PSF photometry. Arrows are labeled with ZAMS masses along the isochrone.

is steeper than any of the average curves derived for various parts of the LMC by Fitzpatrick (1985) or Fitzpatrick & Savage 1984); e.g., $R_{162} = 8.49$ for most of the LMC, and $R_{162} = 9.93$ for the 30 Dor region (Hill et al. 1993a). However, Fitzpatrick (1985) does find one star (Sk −52°71) with a normalized far-ultraviolet extinction approximating our estimate for LH 52. Moreover, the estimate of R_{162} depends on the amount of extinction attributed to the Galactic foreground. If this amount is set to 0, our algorithm estimates $R_{162} \approx 11$, which is near the maximum found by Fitzpatrick (1985) for the 30 Dor region. In any case, the IMF results given below in § 5 are independent of the far-ultraviolet reddening model.

4.2. *LH 53*

We analyze only a portion of LH 53 as defined by Lucke (1972). The UIT supporting images do not include the northernmost ~2′, and we ignore a thin strip of LH 53 that surrounds LH 52 on the west, south, and east. The resulting *C-M* diagram of 2227 stars in LH 53 is shown in Figure 7. Overplotted is a 10 Myr isochrone (see § 5.2) reddened by $E(B-V) = 0.14$, which is computed relative to the isochrone as described in § 4.1, using 425 stars along the main sequence with $17.2 \lesssim V \lesssim 18.7$ and $-0.3 \lesssim B-V \lesssim 0.3$. The 1 σ scatter in stellar $E(B-V)$-values is $\pm$ 0.13.

The *C-M* diagram of LH 53 (Fig. 7) has twice as many stars as that of LH 52 (Fig. 4). However, LH 53 has fewer stars than LH 52 in the region $14 < V < 16$, $B-V < 0.4$. Though LH 53 appears less densely populated in all bandpasses than LH 52 (Fig. 1), it includes the open cluster SL 463 (Hodge & Wright 1967), which suggests the possibility of recent episodes of star formation. A separate *C-M* diagram for a region of ~1 arcmin² including SL 463 is shown in Figure 8 together with the 10 Myr isochrone. SL 463 appears to be approximately the same age as the rest of LH 53. SL 463 is probably an "OB cluster." According to Garmany (1994), groups of this type are properly regarded as "subclusters" of the association, "not to be confused with classical Galactic clusters."

Figure 9 shows the 2-C diagram and ultraviolet-optical *C-M* diagram for LH 53. Isochrones and reddening vectors are plotted as described for Figure 5. The stars in LH 53 are con-

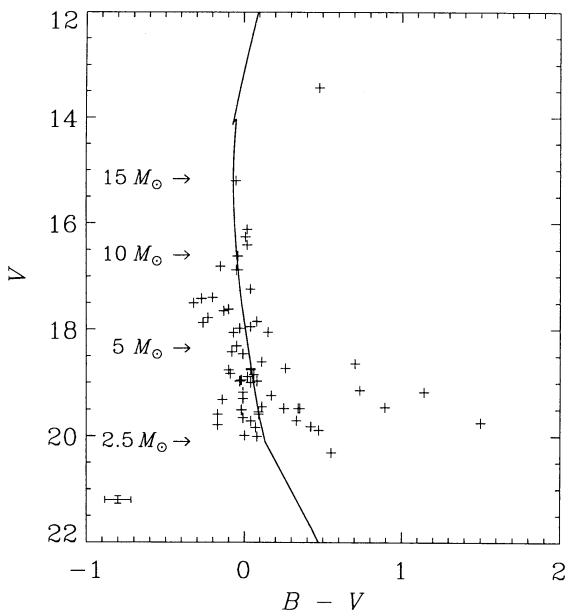

FIG. 8.—*C-M* diagram for a subset of LH 53 stars in 1 arcmin² region surrounding the "OB cluster" SL 463. Isochrone for 10 Myr overplotted as in Fig. 7.

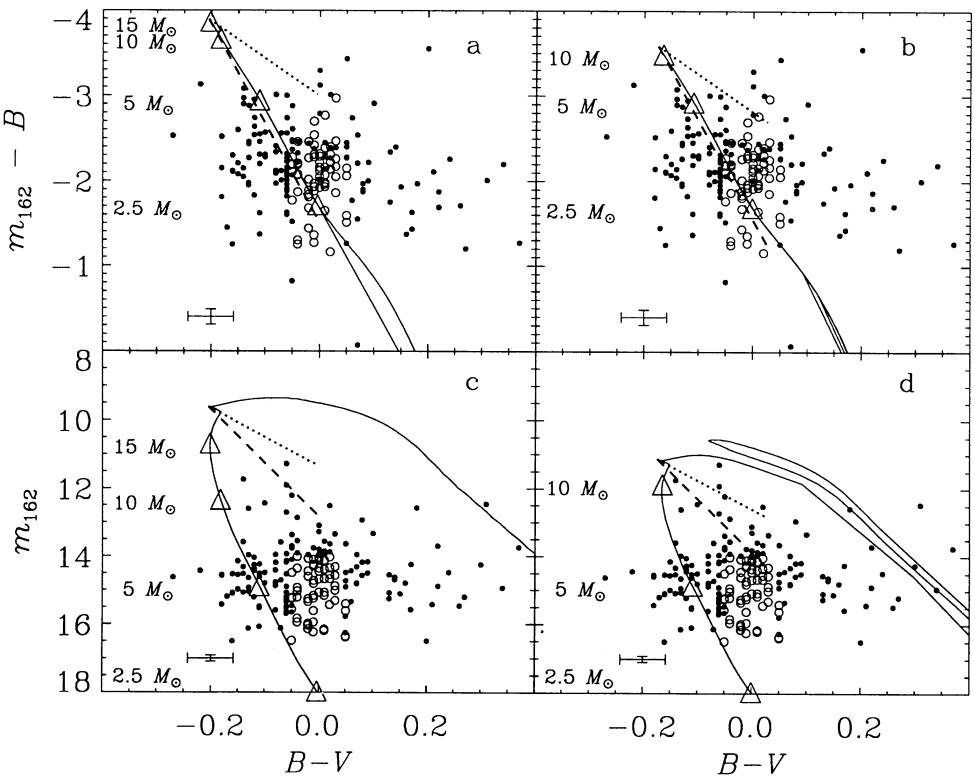

FIG. 9.—2-C diagram and *C-M* diagram of LH 53. *Top row*, $(B-V, m_{162}-B)$ 2-C diagram with (*a*) 10 Myr and (*b*) 20 Myr isochrones. *Bottom row*, $(B-V, m_{162})$ *C-M* diagram with (*c*) 10 Myr and (*d*) 20 Myr isochrones. *Open circles*, Arbitrary group of stars showing the relationship between the *C-M* diagram and the 2-C diagram. *Open triangles*, ZAMS masses given by the labels along the left edge inside each plot. *Error bars*, Mean internal errors from PSF photometry. *Dotted lines*, Reddening vectors for $E(B-V) = 0.2$, LMC reddening curve of Fitzpatrick (1985). *Dashed lines*, Reddening vectors for $E(B-V) = 0.2$, SMC reddening curve of Hutchings (1982).

centrated in a fainter range of m_{162} than those in LH 52. An analysis of V-band luminosity functions (LFs) in the next section explains this effect by showing that LH 53 has more field-star contamination than LH 52, and that LH 53 has a steeper IMF than LH 52.

5. IMF SLOPES

5.1. *Observed Main-Sequence LFs*

Our computation of IMF slopes in LH 52 and LH 53 follows the same outline as those of Mateo (1988) and VBD93. The starting point is the observed main-sequence LF in apparent V magnitude. After being corrected for photometric incompleteness, field-star contamination, and extinction, the LF is converted to a present-day zero-age mass function (PDZAMF) using a theoretical isochrone and an appropriate set of stellar atmosphere models. A power-law distribution of masses is estimated from the PDZAMF by a least-squares fit. The resulting exponent is assumed to be the slope of the IMF of all the association stars that existed originally, i.e., before the demise of the stars having the highest initial masses. Thus, the LF is used to derive a PDZAMF, which then is used to make an inference about the IMF.

The IMF slope is defined (Scalo 1986) as

$$\Gamma \equiv \frac{d \log \xi(\log M)}{d \log M},$$

where ξ is the surface density of stars per kpc^2 per log mass interval and M is zero-age main-sequence (ZAMS) mass in $M_\odot$. In terms of other notations found in the literature, $\Gamma = -x + 1 = \gamma + 1$; the Salpeter (1955) slope is $\Gamma = -1.35$.

The optical LFs discussed in this paper are restricted to the main sequence, which is defined according to the optical *C-M* diagram as including all stars with $B-V \lesssim 0.6$. The actual boundary is not at a constant color index, but rather, it is slanted somewhat in order to coincide with the one delineated by VBD93. Figure 10 compares the LF of LH 52 in V magnitude from the UIT supporting data with one based on the data of VBD93 for the same sky area. In the magnitude range $16 < V < 19$, the two LFs match closely. Thus, VBD93's LF is confirmed by ours, though, of course, the photometric calibrations are not independent. For $V < 16$, the apparent difference between the two LFs results from small-number statistics and is not significant. For $V > 19$, the UIT supporting data are incomplete.

The completeness ratio as a function of magnitude is estimated for our B and V data using the false-star recovery method (Mateo 1988; Stetson & Harris 1988). Many variants of this basic idea are feasible. In the present case, since we are mostly interested in the main sequence, we set $B-V = 0$ for all the false stars. The magnitudes are distributed as the brighter half of a Gaussian with $\mu = 20.5$ and $\sigma = 3.0$, and the positions of the false stars are distributed randomly within the association boundary. We run the point-source detection filter on both the B and the V image, and the resulting detections are cross-matched between the two bandpasses without distinguishing between false and true stars. The resulting list of matches is then cross-matched in turn with the input list of

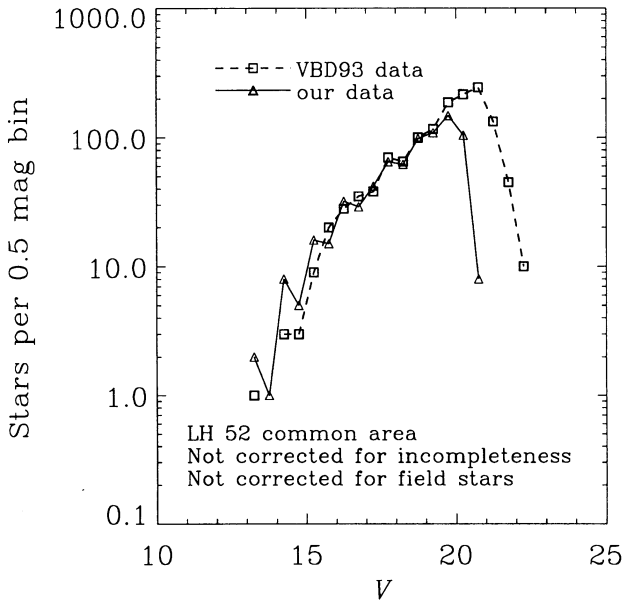

FIG. 10.—Comparison of apparent V LFs from our data and from VBD93 data, no corrections. *Boxes*, VBD93; *triangles*, UIT supporting. Both data sets are restricted to the overlap between LH 52 and the observed fields of VBD93.

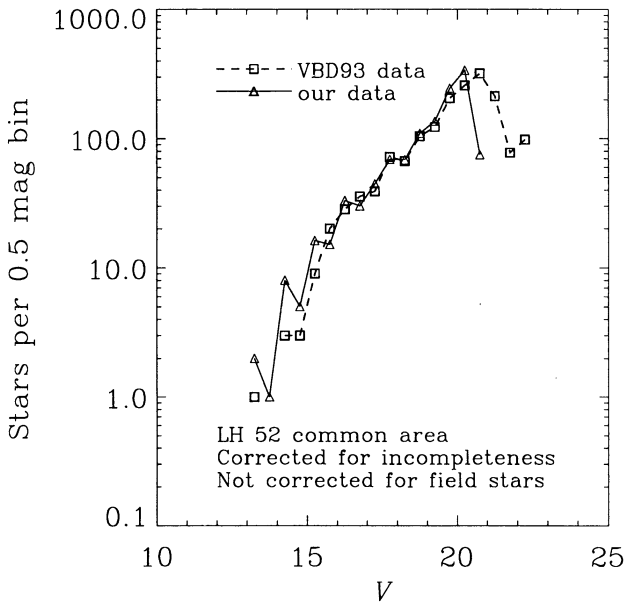

FIG. 12.—Comparison of apparent V LFs from our data and from VBD93 data, as corrected for photometric incompleteness. *Boxes*, VBD93; *triangles*, UIT supporting data. Both data sets are restricted to the overlap between LH 52 and the observed fields of VBD93.

false stars to give the count of stars recovered. The algorithm is run 100 times with a different random set of 20 false stars in each run, for a total of 2000 false stars. The completeness curves that result are shown in Figure 11 for both LH 52 and LH 53.

The reliability of the false-star recovery method is assessed by comparing the completeness-corrected LF from the UIT supporting data with the equivalent LF from the data of VBD93, who use a somewhat different version of the false-star method. This comparison is shown in Figure 12 using the area

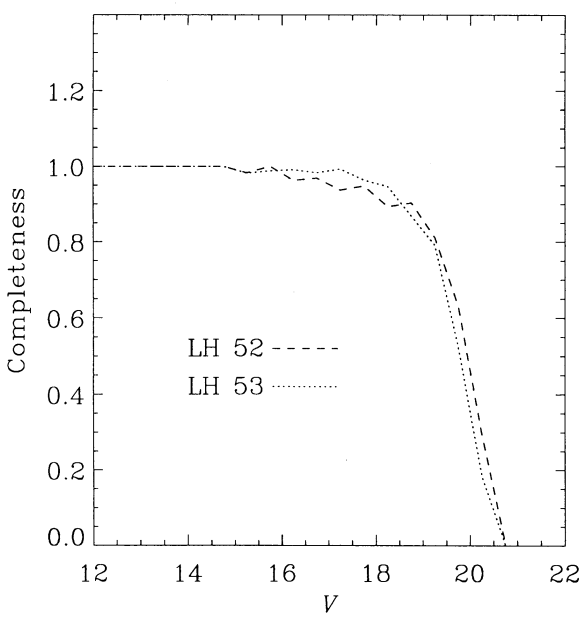

FIG. 11.—Completeness curves for optical photometry of LH 52 (*dashed line*) and LH 53 (*dotted line*) vs. apparent V magnitude. Completeness is assumed to be 1 for $V < 12$.

of LH 52 that is common between the two data sets. The greatest disagreement between the two LFs is in the faintest magnitude bin with significant UIT supporting data; i.e., for $20 \leq V \leq 20.5$, our corrected count is greater than the VBD93 count by a factor of ~ 1.3. The completeness ratio for the UIT supporting data in this bin is 0.3. The adjacent, brighter bins are discrepant by smaller amounts in the same sense. Thus, a systematic difference exists between our incompleteness correction and that of VBD93. In order to minimize the contribution of systematic error, our analysis is restricted to bins with $V \leq 19$, for which the completeness ratios are greater than 0.9.

The population of stars in the general field is assumed to be represented by VBD93's area F1 with a completeness correction read from their Figure 5. Prior to subtraction from the LF of each association, the LF for area F1 is multiplied by the appropriate ratio of solid angles. Because LH 53 subtends ~ 3 times the solid angle of LH 52 and has a lower surface density of stars than LH 52, it contains a greater proportion of field stars than does LH 52.

Figures 13 and 14 show our main-sequence LFs for LH 52 and LH 53, corresponding to the sky areas defined in § 4, i.e., not restricted to the area covered by VBD93. The LFs in Figure 13 are raw star counts, whereas those in Figure 14 are the corrected versions. Even after being corrected for field stars, LH 53 has an excess of low-luminosity stars and a deficit of high-luminosity stars relative to LH 52. This effect is consistent either with a greater average age for the stars in LH 53 or with a steeper IMF for LH 53.

5.2. *Simultaneous Estimates of Age and IMF Slopes*

In order to choose isochrones with which to fit Γ for LH 52 and LH 53, we must first do a preliminary search of the parameter space. Model LFs in V are constructed according to each set of parameter values, and these are compared to the observed LFs using the Kolmogorov-Smirnov (K-S) test (Press et al. 1992). An isochrone of the most likely age for each associ-

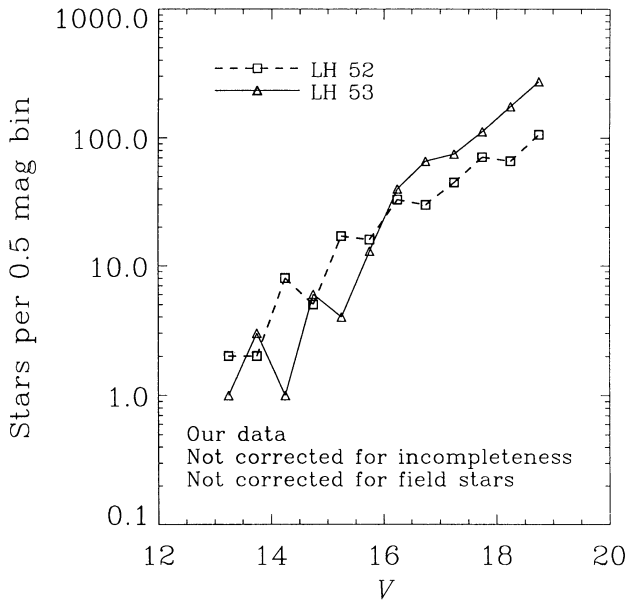

FIG. 13.—Comparison of apparent V LFs for LH 52 and LH 53 without any correction of the star counts in each magnitude bin.

ation is then used to estimate the initial stellar masses for a straightforward fit of the IMF slope. The final fit and its results are described in the next section; here we present in detail the information yielded by the preliminary run of K-S tests.

In order to give a rough idea of the star formation history, the model LFs are formed by addng two components of different ages. We assume the same number of stars and the same IMF slope for both components. In addition, we apply $E(B-V) = 0.15$ for LH 52 and 0.14 for LH 53, of which $E(B-V) = 0.05$ is attributed to the Galactic foreground and the rest, for both associations, is characterized by $R_{162} = 12.6$

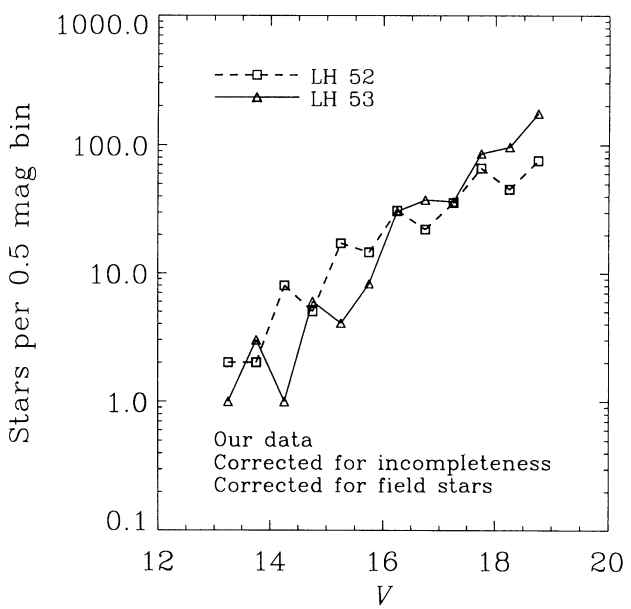

FIG. 14.—Comparison of apparent V LFs for LH 52 and LH 53. Corrected for field-star contamination using VDB93 field F1. Corrected for photometric incompleteness using false-star recovery method.

(§ 4). The ages are taken from the set 5, 10, 15, ..., 35 Myr. For each age pair, we test three different values of Γ, i.e., -1.0, -1.5, and -2.0. This entire set of K-S tests is run twice for each association. In the first run, the observed LFs are used without modification. In the second run, the observed LFs are corrected for photometric incompleteness and field-star contamination. The results are given in Tables 4 and 5, respectively. The goodness of fit is expressed by the statistic P_{KS}; $0 \leq P_{KS} \leq 1$, where 0 signifies the worst fit, and 1 signifies the best fit.

Table 4 gives the results of fitting age pairs and IMF slopes to the uncorrected LFs. Both LH 52 and LH 53 apparently have a significant number of field stars with age $\gtrsim 20$ Myr. Nevertheless, a difference is found between the IMF slopes for the two associations. The LF of LH 52 is fitted fairly well by $\Gamma = -1$ for several pairs of ages, but is incompatible with $\Gamma = -2$. However, for LH 53, both $\Gamma = -1.5$ and $\Gamma = -2$ are possible, whereas $\Gamma = -1$ is ruled out. Table 5 gives the results of the same procedure done using the corrected LFs. For LH 52, the best-fit age pair is (10, 5) Myr with $\Gamma = -1$. For LH 53, though local maxima in P_{KS} are found for the age pairs (30, 20) and (25, 25) Myr with $\Gamma = -1.5$, the best fit is given by (10, 10) Myr with $\Gamma = -2$. In summary, we find a real difference in IMF slopes between LH 52 and LH 53 of $\Delta\Gamma \approx 1$, and both associations are most likely ~ 10 Myr old. Since the initial mass of a star with a 10 Myr lifetime is $\sim 20\ M_\odot$, we cannot determine the upper mass cutoff of the IMF, which is probably at least $\sim 80\ M_\odot$ (Garmany 1993).

The area of the LMC discussed in this paper is interesting because it includes part of the supergiant shell LMC 4 surrounding Shapley constellation III (Goudis & Meaburn 1978), and because of the evidence of Dopita, Mathewson, & Ford (1985) that the history of the entire LMC 4 region conforms to a scenario of stochastic self-propagating star formation. Dopita et al. derive a starting time of 15 Myr ago for the "seed" event at the center of Shapley III, which is inconsistent with an age of 10 Myr for LH 52 and LH 53, as pointed out by VBD93, who suggest modifications to the scenario: a nonconstant propagation velocity leading to an age greater than 15 Myr for the seed event, and a contribution to the gas compression in the N49 region by the adjacent supergiant shell LMC 5.

5.3. *Computing an IMF Slope for a Single Age*

If a single age is assumed for each association, the IMF slope can be computed by a least-squares fit to the PDZAMF. One simple method of computing the PDZAMF is to multiply the extinction-corrected LF by the derivative of the mass-luminosity relation implied by the adopted isochrone (Mateo 1988). However, a method is available that does not require the computation of this derivative. First, the isochrone is transformed to the observational plane using model atmospheres, the distance modulus of the LMC, and the foreground extinction. Second, each point in the C-M diagram is projected onto the isochrone along the appropriate LMC reddening line. The projected point is used to interpolate a ZAMS mass for the star, and the PDZAMF is given by the resulting distribution of masses. This method is implemented in the MOVESTAR algorithm.

To test our method, we apply it to the photometry of VBD93. For comparison with VBD93's result, all of the fields F3, F4, and F5 are used rather than just the area of LH 52. Incompleteness corrections are read from Figure 5 of VBD93; the method of applying them is to weight each star included in

TABLE 4

SIMULTANEOUS FIT OF AGE AND IMF SLOPE, UNCORRECTED

AGE PAIR (Myr)		P_{KS}[a]					
		LH 52			LH 53		
		$\Gamma = -1$	$\Gamma = -1.5$	$\Gamma = -2$	$\Gamma = -1$	$\Gamma = -1.5$	$\Gamma = -2$
5	5.....	0.001	0.544	0.000	0.000	0.000	0.151
10	5.....	0.089	0.128	0.000	0.000	0.000	0.308
10	10.....	0.578	0.017	0.000	0.000	0.000	0.552
15	5.....	0.435	0.016	0.000	0.000	0.000	0.587
15	10.....	0.938	0.001	0.000	0.000	0.003	0.606
15	15.....	0.438	0.000	0.000	0.000	0.018	0.136
20	5.....	0.773	0.004	0.000	0.000	0.002	0.716
20	10.....	0.819	0.000	0.000	0.000	0.015	0.460
20	15.....	0.170	0.000	0.000	0.000	0.069	0.098
20	20.....	0.034	0.000	0.000	0.000	0.213	0.061
25	5.....	0.952	0.001	0.000	0.000	0.007	0.726
25	10.....	0.421	0.000	0.000	0.000	0.071	0.252
25	15.....	0.043	0.000	0.000	0.000	0.251	0.038
25	20.....	0.010	0.000	0.000	0.000	0.580	0.022
25	25.....	0.001	0.000	0.000	0.003	0.947	0.003
30	5.....	0.950	0.001	0.000	0.000	0.016	0.538
30	10.....	0.227	0.000	0.000	0.000	0.185	0.147
30	15.....	0.015	0.000	0.000	0.000	0.519	0.020
30	20.....	0.003	0.000	0.000	0.002	0.895	0.012
30	25.....	0.000	0.000	0.000	0.012	0.898	0.003
30	30.....	0.000	0.000	0.000	0.037	0.647	0.001
35	5.....	0.824	0.000	0.000	0.000	0.037	0.438
35	10.....	0.126	0.000	0.000	0.000	0.238	0.097
35	15.....	0.007	0.000	0.000	0.000	0.597	0.013
35	20.....	0.001	0.000	0.000	0.003	0.943	0.008
35	25.....	0.000	0.000	0.000	0.025	0.634	0.002
35	30.....	0.000	0.000	0.000	0.092	0.395	0.001
35	35.....	0.000	0.000	0.000	0.140	0.204	0.001

[a] Goodness-of fit statistic derived from observed LF in the V bandpass; 0 is worst fit, and 1 is best fit.

the computed PDZAMF by the reciprocal of the completeness ratio for its apparent magnitude. The field-star correction is done by computing a PDZAMF from VBD93 field F1 using the same isochrone-projection method as for the association fields, then subtracting this PDZAMF from the association IMF with an area scaling. The field-star PDZAMF is used only for this correction; it does not describe the actual distribution of ZAMS masses in F1, because in general, the isochrone age is inappropriate.

Fitting is done in the logarithm of the quantity ξ to obtain the slope Γ (§ 5.1). Every bin has the width 0.1 in log $M_\odot$. Errors are derived from the counting statistics in each mass bin and are forced to be symmetric in the logarithm of the star count. The fit is weighted by the reciprocal of the error in each bin. The justification for this use of counting statistics is as follows. The slope Γ is regarded as a unique function of unknown physical variables. Thus, the IMF, parametrized by Γ, is an idealized parent population from which any star formation episode represents a sampling. In this sense, the formation of a particular set of stars is *part of the observation.* The finitude of the star counts creates error in the estimate of Γ, even if the photometry is perfectly complete. This kind of error is taken into account by using counting statistics in the fit.

For the ZAMS mass range 3.5–12.6 $M_\odot$, we obtain $\Gamma = -1.04 \pm 0.17$ from the VBD93 data. The result obtained by VBD93 for convective overshoot models with no binary-star correction is $\gamma = -2.00 \pm 0.3$ for the same mass range, or $\Gamma = -1.00$. Thus, the method described here is in excellent agreement with that of VBD93.

A PDZAMF of LH 52 is shown in Figure 15. This PDZAMF is made from UIT supporting data in B and V using a 10 Myr isochrone. Also shown is a PDZAMF made similarly from the cross-matched ultraviolet and B photometry. Figure 16 is the equivalent plot for LH 53, also computed using a 10 Myr isochrone. Overplotted on Figures 15 and 16 are the lines resulting from least-squares fits. The fit results are listed in Table 6, which gives the values of Γ computed for LH 52 and LH 53 with both the incompleteness correction and the field-star correction. No correction is made for binaries. Ages of both 10 Myr and 25 Myr are tested for LH 53. The results show that the IMF slope of LH 53 is steeper than that of LH 52 by a difference $\Delta\Gamma \approx 1$, with little dependence on the assumed age of LH 53. Where the UIT data are complete (above 10 $M_\odot$), they confirm the existence of a striking difference in IMF slopes between the two associations.

This difference in IMFs is similar to a result of Parker et al. (1992) on the young (age <5 Myr) associations LH 9 and LH 10 in the northwestern part of the LMC. Parker et al. find that the older association, LH 9, has a steeper IMF than the younger association, LH 10, by $\Delta\Gamma = 0.5$. Moreover, the slope for the younger association, LH 10, is $\Gamma \approx -1$, just as for LH 52. The physical inference drawn by Parker et al. is that the

TABLE 5

SIMULTANEOUS FIT OF AGE AND IMF SLOPE, CORRECTED FOR INCOMPLETENESS AND FIELD STAR CONTAMINATION

AGE PAIR (Myr)		P_{KS}[a]					
		LH 52			LH 53		
		$\Gamma = -1$	$\Gamma = -1.5$	$\Gamma = -2$	$\Gamma = -1$	$\Gamma = -1.5$	$\Gamma = -2$
5	5.....	0.049	0.001	0.000	0.000	0.000	0.227
10	5.....	0.673	0.000	0.000	0.000	0.000	0.522
10	10.....	0.309	0.000	0.000	0.000	0.000	0.731
15	5.....	0.397	0.000	0.000	0.000	0.000	0.688
15	10.....	0.033	0.000	0.000	0.000	0.001	0.249
15	15.....	0.001	0.000	0.000	0.000	0.008	0.039
20	5.....	0.102	0.000	0.000	0.000	0.001	0.343
20	10.....	0.004	0.000	0.000	0.000	0.007	0.094
20	15.....	0.000	0.000	0.000	0.000	0.035	0.013
20	20.....	0.000	0.000	0.000	0.000	0.122	0.002
25	5.....	0.034	0.000	0.000	0.000	0.005	0.211
25	10.....	0.001	0.000	0.000	0.000	0.035	0.052
25	15.....	0.000	0.000	0.000	0.000	0.146	0.006
25	20.....	0.000	0.000	0.000	0.000	0.388	0.001
25	25.....	0.000	0.000	0.000	0.001	0.489	0.000
30	5.....	0.014	0.000	0.000	0.000	0.020	0.157
30	10.....	0.000	0.000	0.000	0.000	0.110	0.033
30	15.....	0.000	0.000	0.000	0.000	0.338	0.003
30	20.....	0.000	0.000	0.000	0.001	0.682	0.001
30	25.....	0.000	0.000	0.000	0.006	0.287	0.000
30	30.....	0.000	0.000	0.000	0.029	0.144	0.000
35	5.....	0.004	0.000	0.000	0.000	0.027	0.095
35	10.....	0.000	0.000	0.000	0.000	0.137	0.018
35	15.....	0.000	0.000	0.000	0.000	0.402	0.001
35	20.....	0.000	0.000	0.000	0.001	0.480	0.000
35	25.....	0.000	0.000	0.000	0.012	0.174	0.000
35	30.....	0.000	0.000	0.000	0.048	0.081	0.000
35	35.....	0.000	0.000	0.000	0.076	0.040	0.000

[a] Goodness-of-fit statistic derived from observed LF in the V bandpass; 0 is worst fit, and 1 is best fit.

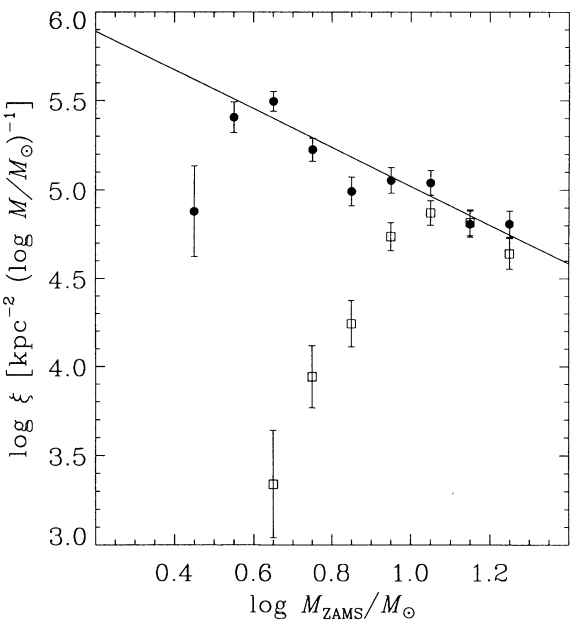

FIG. 15.—LH 52 PDZAMFs, assuming an age of 10 Myr. *Filled circles*, Computed from $(B-V, V)$ *C-M* diagram, corrected for field-star contamination and incompleteness; *squares*, computed from $(m_{162} - B, B)$ *C-M* diagram, no corrections. Error bars are from counting statistics and are forced to be symmetrical in the log. *Solid line*, Fitted IMF with a slope of $\Gamma = -1.09$.

older association preconditions the environment in which the younger association forms, and perhaps the older association triggers the star formation in the younger association. This picture is plausible for LH 9 and LH 10 because the age difference between them is relatively small; from Figures 12 and 13 of Parker et al. (1992), the difference may be as little as 1 Myr. If LH 52 and LH 53 are nearly equal in age, as implied by the age-IMF fit above, their situation is remarkably similar to that of LH 9 and LH 10.

A related instance is discussed by Hill et al. (1994), who compare several associations in the UIT field surrounding 30 Dor to the field in which they are embedded. For stars within the association boundaries (Lucke 1972), Hill et al. find $\Gamma = -1.08 \pm 0.2$; for stars in the field, they find $\Gamma = -1.74 \pm 0.3$, comparable to the slopes found by us for LH 52 and LH 53, respectively. Figure 1 of Hill et al. (1994) shows that the distribution of hot stars formally outside the

TABLE 6

IMF SLOPES OF LH 52 AND LH 53

Association	Age (Myr)	Fitted Masses ($M_\odot$)	Γ
LH 52.....	10	4.0–20.0	-1.09 ± 0.12
LH 53.....	10	4.0–20.0	-1.92 ± 0.12
LH 53.....	25	4.0–12.6	-2.13 ± 0.29

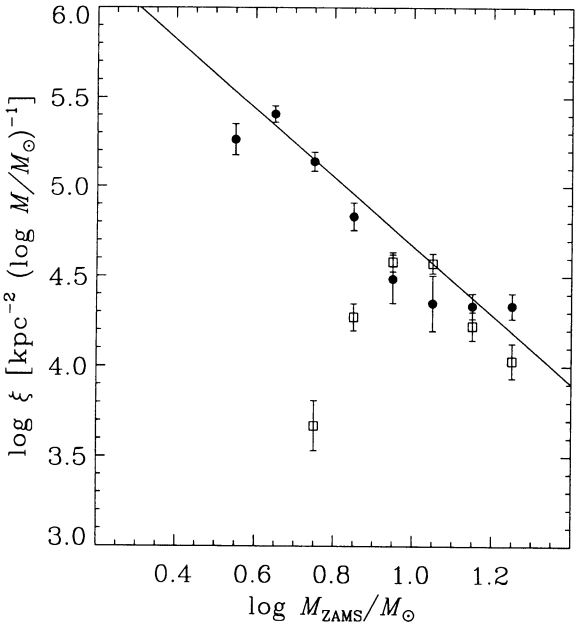

FIG. 16.—LH 53 PDZAMFs, assuming an age of 10 Myr. *Filled circles*, Computed from $(B-V, V)$ *C-M* diagram, corrected for field-star contamination and incompleteness; *squares*, computed from $(m_{162}-B, B)$ *C-M* diagram, no corrections. Error bars are from counting statistics and are forced to be symmetrical in the log. *Solid line*, Fitted IMF with a slope of $\Gamma = -1.92$.

associations is nonuniform. Indeed, three of the six pictured associations (LH 90, 97, and 104) are similar to LH 52 in that they appear to be the most concentrated portions of larger groups, so that they are in the same relationship to their surroundings as LH 52 is to LH 53. The apparent pattern of the results for both the 30 Dor region and the region discussed in this paper is that a high surface density of stars detected in the ultraviolet implies a relatively flat IMF.

6. N49

N49 is an SNR of age $\sim 10^4$ yr that is well studied at both ultraviolet and optical wavelengths (e.g., Vancura et al. 1992a—hereafter VBLR—1992b; Shull 1993; Shull et al. 1985; Osterbrock & Dufour 1973). The UIT 162 nm image of N49 is shown in Figure 17*a*. The emission is dominated by the two bright features marked A and B. Ultraviolet fluxes for these two features, as well as for the SNR as a whole, are given in Table 7.

TABLE 7

ULTRAVIOLET FLUX OF N49

FEATURE[a]	COORDINATES (J2000) α	δ	r[b]	162 nm FLUX[c]
A.....	5^{h}26^{m}03^s.57	−66°05′05″.8	13.1	3.12×10^{-14}
B.....	5 26 02.48	−66 05 26.4	9.4	1.08×10^{-14}
N49.....	5 26 01.34	−66 05 05.6	41.0	1.10×10^{-13}

[a] See Fig. 17.
[b] Radius of circular aperture in arcseconds.
[c] In ergs cm^{-2} Å^{-1} in the UIT B5 filter, calibrated using *IUE* spectra enumerated in VBLR.

Figure 17*b* shows the UIT B5 image co-aligned with X-ray contours from the *Einstein* high-resolution imager (HRI). The brightest X-ray emission lies between and slightly to the east of ultraviolet features A and B. Possibly, this set of features represents a cloud encountered by the SNR blast wave. If so, the X-ray maximum is from gas in the cloud behind the blast wave, and the two ultraviolet features are from radiative reflected shocks, also in the cloud, which are propagated back in the direction of the center of the remnant. Such a scenario is proposed by Hester & Cox (1986) to explain the relationship between [O III] and X-ray emission in the northeastern Cygnus Loop. The UIT data on the Cygnus Loop are consistent with this picture, since the ultraviolet emission is due mainly to C IV λ1550, which is typically produced in the same regions as [O III], over a broad range of shock velocities greater than 100 km s^{-1} (Cornett et al. 1992).

In N49, the brightest ultraviolet and [O III] features differ in detail, though they follow each other in general. Figure 17*c* depicts the *Einstein* contours superposed on a version of VBLR's [O III] image (kindly supplied by W. P. Blair). This image is smoothed to UIT resolution (~4″); the alignment

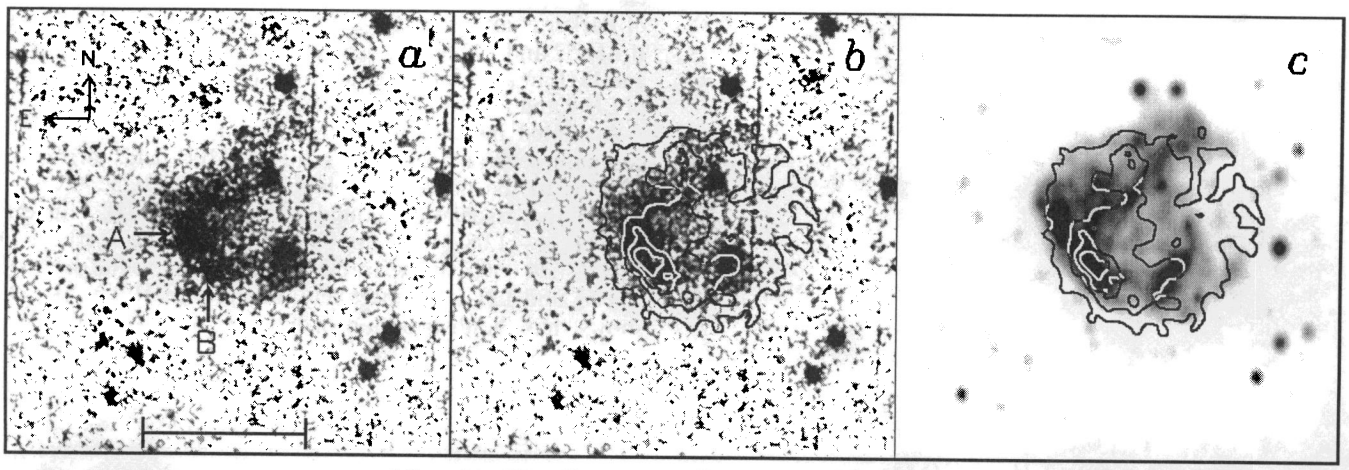

FIG. 17.—(*a*) UIT image of N49 (cf. Fig. 1) with linear intensity scaling. Scale is 1′. Features A and B are discussed in the text. (*b*) UIT image overlaid with *Einstein* HRI contours. HRI image smoothed by Gaussian of 4″.1 FWHM, then contoured at levels of 1, 3, 5, and 7 counts. A bright X-ray feature is straddled by ultraviolet feature A and B. (*c*) HRI contours overlaid on VBLR's [O III] image, smoothed to UIT resolution. Bright [O III] emission extends to the northeast of ultraviolet feature A, though in general the [O III] and ultraviolet emission coincide. Co-alignment of X-ray and [O III] images is done following VBLR, then ultraviolet is aligned with [O III] using stars.

follows VBLR. Comparison with Figures 17*a* and 17*b* shows a bright extension of the [O III] emission toward the northeast from ultraviolet feature A.

Cornett et al. (1992) explain such a partial correspondence between [O III] and the 162 nm band in the Cygnus Loop as the result of the greater absorption coefficient in the C IV λ1550 resonance lines than in [O III] $\lambda\lambda$4959, 5007. In this SNR, the 162 nm band is evidently dominated by C IV, and shock models show the same effect for a range of velocities (Cornett et al. 1992). Although C IV and [O III] are typically produced together, the emitting gas can be optically thick in C IV but not in [O III]. This case occurs if the line of sight is tangent to part of a geometrically thin, sheetlike emitting region. Thus, changes in the C IV:[O III] ratio are explained by differences in the orientation of shocks in the SNR with respect to the observer.

Although the geometric explanation for the observed relationship of 162 nm intermediate-band emission and [O III] emission seems applicable to the Cygnus Loop, the situation in N49 differs. The approximation of treating the 162 nm emission essentially as C IV is not reasonable for N49, where the UIT B5 band includes substantial contributions from other species, such as He II λ1640 and O III λ1663. Moreover, much of the UIT B5 flux is contributed by continuum. Interpolating over relatively line-free segments of *IUE* spectrum SWP 36372 (VBLR's position A) shows that 0.6 of the total flux in the B5 band is continuum, probably from the hydrogen two-photon process (VBLR; Benvenuti, Dopita, & d'Odorico 1980). The ratio of C IV to two-photon continuum from this position in N49 is lower than the same ratio at three Cygnus Loop positions observed by Raymond et al. (1988) by factors of 1.6, 5.6, and 12.8, respectively. Therefore, differences between the 162 nm and the [O III] morphology of N49 cannot be attributed to C IV with as great a confidence as in the Cygnus Loop.

From the Balmer decrement of N49, VBLR derive a reddening of $E(B-V) = 0.37$. Vancura et al. (1992b) find an intrinsic variation in the reddening of ± 0.14, which is the 1 σ scatter among $2'' \times 2''$ apertures. These estimates can be compared with ones derived from the stellar photometry and the 10 Myr isochrone as described above. From *B* and *V* photometry of 19 main-sequence stars in a $70'' \times 70''$ box including N49, $E(B-V) = 0.23 \pm 0.29$, including both Galactic and LMC reddening. From 162 nm and *B* photometry of three stars in and near N49, $E(B-V) = 0.19 \pm 0.04$. The errors are 1 σ scatter. Thus, we find a distribution of $E(B-V)$ with a lower mean and a larger dispersion than that found by VBLR. However, there is no real inconsistency between the two measurements, since our samples are probably biased toward stars lying in front of the SNR, especially in the case of the three ultraviolet-detected stars.

The age of the most recent star formation in LH 53 is $\sim$10 Myr, according to the LF fits (§ 5.2), with a weak probability of $\sim$25 Myr. From an interpolation using the evolutionary tracks of Schaerer et al. (1993), the ZAMS mass of a star with a 25 Myr lifetime is 10.3 $M_\odot$, which implies a spectral type of B3 for the progenitor star (Mihalas & Binney 1981). For a star with a 10 Myr lifetime, the ZAMS mass is 19.9 $M_\odot$, corresponding to a spectral type of O9. Thus, the assumption of Shull et al. (1985) that the progenitor was an "early B" star is consistent with our data on LH 53.

7. CONCLUSIONS

The parameters of each association—which include the age of last star formation, the duration of star formation, the IMF slope, the extinction, the reddening curve, and the metallicity—are coupled and cannot all be constrained at once using the data in this paper. However, provisional conclusions are made possible by restricting the parameter space. For example, we assume a metallicity of 0.5 $Z_\odot$, and when convenient, we assume a single age for each association.

The principal conclusion is that the association LH 53 has an IMF steeper than that of LH 52 by $\Delta\Gamma \approx 1$. In addition, we find that the reddening curve in LH 52 is steeper in the far-ultraviolet than the 30 Dor curve of Fitzpatrick (1985). The reddening internal to the LMC in our field is low at $E(B-V) = 0.10$ for LH 52 and $E(B-V) = 0.09$ for LH 53.

The difference in Γ between LH 52 and LH 53 is similar to the difference between associations near 30 Dor and the stars in the surrounding UIT field found by Hill et al. (1994). Another such case is that of LH 9 and LH 10 observed by Parker et al. (1992). Taken together, all these results suggest that the IMF slope is not a universal parameter, but is determined by local physical conditions. Furthermore, the slope is apparently correlated with the observed surface density of stars in the sence that a high density implies a shallow slope.

The reddening in the neighborhood of the SNR is lower according to our data than the value found by VBLR for the SNR itself. However, the scatter in reddening is twice that found by VBLR. The 162 nm UIT image of N49, dominated by hydrogen two-photon continuum and by C IV λ1550 line emission, shows two bright regions straddling an X-ray bright feature seen in the *Einstein* HRI image. This complex may represent an encounter of the blast wave with a cloud, according to the type of scenario used by other investigators (Hester & Cox 1986; Cornett et al. 1992) in the case of the Cygnus Loop.

The best-fit age of LH 52 is $\sim$10 Myr, in agreement with VBD93. The best-fit age of LH 53 is also $\sim$10 Myr. These results support the modification by VBD93 to the history of supergiant shell LMC 4 proposed by Dopita et al. (1985), and they also suggest an initial mass of $\sim$20 $M_\odot$ for the N49 progenitor star.

This work was helped by the generosity of D. Bomans and W. P. Blair in sharing and answering questions about their data. We also wish to acknowledge the usefulness of the Wide Area Information Server (WAIS) node of Project STELAR (Code 631, NASA/GSFC) in locating literature references. The *Einstein* image of N49 was obtained from the on-line service EINLINE at the Center for Astrophysics. We thank R. H. Cornett and J. K. Hill for many useful discussions. Funding for the UIT project has been through the Spacelab Office at NASA Headquarters under project 440-51.

REFERENCES

Benvenuti, P., Dopita, M., & D'Odorico, S. 1980, ApJ, 238, 601
Brunet, J. P. 1975, A&A, 43, 345
Cornett, R. H., et al. 1992, 395, L9
Dopita, M. A., Mathewson, D. S., & Ford, V. L. 1985, ApJ, 297, 599
Fanelli, M. N., O'Connell, R. W., Burstein, D., & Wu, C.-C. 1992, ApJS, 82, 197
Fitzpatrick, E. L. 1985, ApJ, 299, 219
Fitzpatrick, E. L., & Savage, B. D. 1984, ApJ, 279, 578
Garmany, C. D. 1994, PASP, 106, 25

Goudis, C., & Meaburn, J. 1978, A&A, 68, 189
Greason, M. R., Offenberg, J. D., Cornett, R. H., Hill, R. S., & Stecher, T. P. 1994, PASP, 106, 1151
Hartigan, P., Raymond, J. C., & Hartmann, L. 1987, ApJ, 316, 323
Hester, J. J., & Cox, D. P. 1986, ApJ, 300, 675
Hill, J. K., et al. 1993a, ApJ, 413, 604
Hill, J. K., Isensee, J. E., Cornett, R. H., Bohlin, R. C., O'Connell, R. W., Roberts, M. S., Smith, A. M., & Stecher, T. P. 1994, ApJ, 425, 122
Hill, R. S. Hill, J. K., Greason, M. R. 1993b, Ultraviolet Imaging Telescope Batch Data Reduction: Design and Programs (Document HSTX/SES-9301) (Lanham: Hughes STX)
Hodge, P. W., & Wright, F. W. 1967, The Large Magellanic Cloud (Smithsonian Publ. 4699) (Washington, DC: Smithsonian)
Hutchings, J. B. 1982, ApJ, 255, 70
Kurucz, R. L. 1992, in The Stellar Populations of Galaxies, ed. B. Barbuy & A. Renzini (Dordrecht: Kluwer), 225
Lucke, P. B. 1972, Ph.D. thesis, Univ. Washington
Lucke, P. B., & Hodge, P. W. 1970, AJ, 75, 171
Mateo, M. 1988, ApJ, 331, 261
Mathewson, D. S., Ford, V. L., Dopita, M. A., Tuohy, I. R., Long, K. S., & Helfand, D. J. 1983, ApJS, 51, 345
Mihalas, D., & Binney, J. 1981, Galactic Astronomy: Structure and Kinematics (San Francisco: Freeman)
Osterbrock, D. E., & Dufour, R. J. 1973, ApJ, 185, 441
Parker, J. W., Garmany, C. D., Massey, D., & Walborn, N. R. 1992, AJ, 103, 1205
Press, W. H., Teukolsky, S. A., Vetterling, W. T., & Flannery, B. P. 1992, Numerical Recipes in Fortran (2d ed.; Cambridge: Cambridge Univ. Press), 617
Raymond, J. C., Hester, J. J., Cox, D., Blair, W. P., Fesen, R. A., & Gull, T. R. 1988, ApJ, 324, 869
Salpeter, E. E. 1955, ApJ, 121, 161
Savage, B. D., & Mathis, J. S. 1979, ARA&A, 17, 73
Scalo, J. M. 1986, Fund. Cosmic Phys., 11, 1
Schaerer, D., Meynet, G., Maeder, A., & Schaller, G. 1993, A&AS, 98, 523
Shull, P., Jr. 1983, ApJ, 275, 611
Shull, P., Jr., Dyson, J. E., Kahn, F. D., & West, K. A. 1985, MNRAS, 212, 799
Stecher, T. P., et al. 1992, ApJ, 395, L1
Stetson, P. B. 1987, PASP, 99, 191
Stetson, P. B., & Harris, W. E. 1988, AJ, 96, 909
Vallenari, A., Bomans, D. J., & deBoer, K. S. 1993, A&A, 268, 137 (VBD93)
Vancura, O., Blair, W. P., Long, K. S., & Raymond, J. C. 1992a, ApJ, 394, 158 (VBLR)
Vancura, O., et al. 1992b, ApJ, 401, 220
Westerlund, B. E. 1990, A&A Rev., 2, 29